

Visualization of spin-orbit entangled 4f electrons

Shunsuke Kitou¹, Kentaro Ueda², Yuiga Nakamura³, Kunihisa Sugimoto⁴,
Yusuke Nomura⁵, Ryotaro Arita^{6,7}, Yoshinori Tokura^{2,7,8}, and Taka-hisa Arima^{1,7}

¹*Department of Advanced Materials Science, The University of Tokyo, Kashiwa 277-8561, Japan*

²*Department of Applied Physics, The University of Tokyo, Tokyo 113-8656, Japan*

³*Japan Synchrotron Radiation Research Institute (JASRI), SPring-8, Hyogo 679-5198, Japan*

⁴*Department of Chemistry, Kindai University, Osaka 577-8502, Japan*

⁵*Institute for Materials Research, Tohoku University, Sendai, 980-8577, Japan*

⁶*Department of Physics, The University of Tokyo, Tokyo 113-0033, Japan*

⁷*RIKEN Center for Emergent Matter Science (CEMS), Wako 351-0198, Japan*

⁸*Tokyo College, The University of Tokyo, Tokyo 113-8656, Japan*

Abstract

Electrons in localized 4f orbitals around lanthanide elements in solids are dominated by strong spin-orbit coupling. The resultant J multiplets are further split by the crystalline electric field, where J denotes the total angular momentum quantum number, and hence exhibit anisotropic spatial distribution. The anisotropy of spin-orbit entangled 4f electrons is closely linked to their physical properties. Here, we demonstrate the visualization of 4f electrons in pyrochlore oxides $A_2\text{Ir}_2\text{O}_7$ ($A = \text{Pr}, \text{Nd}, \text{and Eu}$) by combining high-photon-energy X-ray diffraction and valence electron density (VED) analysis based on the core differential Fourier synthesis (CDFS) method. The observed VED distributions around the A site roughly agree with point-charge calculations, considering the relativistic spin-orbit coupling and the trigonal crystal electric field under the LS coupling scheme. The CDFS-based VED observation method can be applied to the analysis of the 4f state of various crystalline materials.

Introduction

Lanthanide compounds have been providing a playground of interesting physical properties such as diverse magnetic structures [1], multipole order [2], and unconventional superconductivity [3,4]. Since 5s and 5p electrons partly shield the effect of surrounding atoms, the 4f electrons on the lanthanide atom hardly participate in chemical bonding with surrounding ions and form J multiplets owing to the strong relativistic spin-orbit coupling (SOC). Crystalline electric field (CEF) from surrounding ions further split the multiplets. The resultant eigenstates have anisotropic spatial distribution and hence can host various multipoles. The wavefunctions and energy levels of the 4f states, determined by SOC and CEF, not only govern the material's magnetization and specific heat but also influence various properties such as magnetic anisotropy, Kondo effect [5], and multipole order/fluctuation [2].

If the spatial distribution of 4f electrons can be visualized, it enables direct understanding of the 4f-electron wavefunction. The 3d electrons in transition metal compounds have been observed by using several techniques [6-10]. In contrast, the methodologies for the experimental observation of 4f electrons are limited [11]. Although inelastic neutron scattering has been the most commonly used method to analyze the 4f level scheme, the wavefunctions estimated by fitting the scattering intensity involve significant ambiguity. The X-ray diffraction is a good candidate for the observation of the spatial distribution of electrons. In fact, the spatial distribution of 3d electrons was successfully observed by cutting-edge analysis of X-ray scattering. For example, the spatial distribution of valence electron density (VED) in various crystalline materials has been visualized by combining high-photon-energy X-ray diffraction and a core differential Fourier synthesis (CDFS) analysis [10,12-18]. Nonetheless, the direct observation of the

spatial distribution of 4f electrons remains a significant challenge because (i) 4f electrons exhibit steeper spatial modulation compared to 3d electrons, demanding higher spatial resolution, and (ii) lanthanide elements accommodate a larger number of core electrons than 3d transition elements, necessitating a wider dynamic range.

In this study, we visualize the 4f VED distribution on the lanthanide ions at the *A* site in pyrochlore oxides $A_2\text{Ir}_2\text{O}_7$ ($A = \text{Pr}, \text{Nd}, \text{and Eu}$) through CDFS analysis using single-crystal high-photon-energy X-ray diffraction. We demonstrate that the 4f state can be determined directly from the anisotropy of the VED distribution. High-photon-energy X-ray diffraction experiments at the synchrotron radiation facility SPring-8 guarantee a spatial resolution of approximately 0.25 Å and a dynamic range of intensity exceeding 10^6 . Furthermore, we provide experimental guidelines for observing 5d electrons using next-generation synchrotron radiation facilities.

Results and discussion

The pyrochlore iridates $A_2\text{Ir}_2\text{O}_7$ ($A = \text{lanthanide}$) with cubic space group $Fd-3m$ [19,20] undergo a transition from an antiferromagnetic insulator/semimetal ($A = \text{Y}, \text{Dy}, \text{Gd}, \text{Eu}, \text{Sm}, \text{Nd}$) to a paramagnetic metal ($A = \text{Pr}$) by replacing *A* ions [21-24], where exotic electronic and magnetic properties such as anomalous Hall effect [25-27], magnetic-field-induced metal-insulator transition [28], spin-liquid behavior [29], and spin-ice-like magnetic order [30] are realized. Figure 1a shows the crystal structure of $A_2\text{Ir}_2\text{O}_7$. The *A*-ion dependence of the crystal structure of $A_2\text{Ir}_2\text{O}_7$ ($A = \text{Eu}, \text{Nd}, \text{and Pr}$) at 100 K is summarized in Fig. S1, where the Ir—O—Ir bond angle governing the magnetic interactions between Ir moments is observed to change systematically with the *A*-ion. The *A* and Ir atoms each form a pyrochlore network. While each Ir atom is surrounded

by six O(1), which form a trigonally distorted octahedron, each A atom is surrounded by eight O, six O(1) and two O(2), as shown in Fig. 1b. The local symmetry at both A and Ir sites is $\bar{3}m$ (D_{3d}). The formal valences of A and Ir are +3 and +4, respectively. For example, in the case of $A^{3+} = \text{Pr}^{3+}$ with $4f^2$ electrons, the orbital and spin angular momentum quantum numbers in the low-lying multiplets are $L = 5$ and $S = 1$, respectively. The total angular momentum quantum number in the ground state is $J = |L - S| = 4$ when considering the SOC under the LS coupling scheme (Fig. 1c). In the trigonal CEF, the $J = 4$ nonuplet 3H_4 is expected to split into three doublets and three singlets. Similarly, for $A^{3+} = \text{Nd}^{3+}$ with $4f^3$ electrons, the $J = 9/2$ decuplet ${}^4I_{9/2}$ should split into five Kramers doublets (Fig. 1d). Figures 1e and 1f show the $4f^2$ and $4f^3$ electron density distributions of eigenstates corresponding to $J_z = \pm 4, \pm 3, \pm 2, \pm 1, 0$, and $J_z = \pm 9/2, \pm 7/2, \pm 5/2, \pm 3/2, \pm 1/2$, respectively. Although the ground state in the CEF can be represented by a linear combination of the J_z eigenstates, experimentally determining the wavefunctions in terms of the anisotropy of the 4f electrons remains challenging.

Figures 1g-1i show the VED distributions around the A = Pr, Nd, and Eu sites, respectively, obtained from the CDFS analysis of $A_2\text{Ir}_2\text{O}_7$ at 100 K. The local Cartesian coordinate system for the A site at $(1/2, 1/2, 1/2)$ is defined as $\mathbf{x} \parallel 2\mathbf{a} - \mathbf{b} - \mathbf{c}$, $\mathbf{y} \parallel \mathbf{b} - \mathbf{c}$, and $\mathbf{z} \parallel \mathbf{a} + \mathbf{b} + \mathbf{c}$. Here, the z-axis is the local three-fold rotation axis and the y-axis is perpendicular to a mirror plane. Anisotropic VED is observed around the Pr site, as shown by yellow iso-density surfaces (Fig. 1g). Around the Nd site, the yellow iso-density surface appears relatively isotropic, while the orange surface, representing a higher density level, exhibits anisotropic distribution (Fig. 1h). In contrast to the two A ions, nearly isotropic VED is observed around the Eu site (Fig. 1i). In the case of Eu^{3+} with $4f^6$ electrons, it is predicted that the total angular momentum quantum number is $J = 0$ and the

VED distribution is spherical, which is consistent with the experimental result.

To quantify the anisotropy of the 4f VED around the Pr and Nd sites, the density $\rho(\theta, \phi)$ at distances $r = 0.33$ and 0.24 Å from the nucleus, corresponding to the peak top of the radial profile of $\rho(r)$ along the a -axis (see Fig. S3), is shown by a color map on a sphere in Figs. 2a and 2b, respectively. The color scale shows $[\rho(\theta, \phi) - \overline{\rho(\theta, \phi)}] / \overline{\rho(\theta, \phi)}$. The anisotropy of VED is greater in Pr³⁺ than in Nd³⁺. The 4fⁿ ground state in the trigonal CEF can be described approximately as a linear combination of different J_z eigenstates in the LS coupling scheme. The trigonal CEF \hat{H}_{CEF} can be expanded [31] as

$$\hat{H}_{\text{CEF}} = B_{20}\hat{O}_{20} + B_{40}\hat{O}_{40} + B_{43}\hat{O}_{43} + B_{60}\hat{O}_{60} + B_{63}\hat{O}_{63} + B_{66}\hat{O}_{66}. \quad (1)$$

Here, B_{lm} and \hat{O}_{lm} are the CEF parameters and the CEF operators, respectively. In the case of 4f² of Pr³⁺, the $J = 4$ nonuplet is split into three doublets and three singlets, as shown in Fig. 1c. The doublets and singlets can be represented as

$$|\Gamma_{\alpha} \pm\rangle = C_1|J_z = \pm 4\rangle + C_2|J_z = \pm 1\rangle + C_3|J_z = \mp 2\rangle, \quad (|C_1|^2 + |C_2|^2 + |C_3|^2 = 1) \quad (2)$$

and

$$|\Gamma_{\beta} \pm\rangle = C_4|J_z = \pm 3\rangle + C_5|J_z = 0\rangle + C_6|J_z = \mp 3\rangle, \quad (|C_4|^2 + |C_5|^2 + |C_6|^2 = 1) \quad (3)$$

respectively. Here, double-sign corresponds. In the case of 4f³ of Nd³⁺, the $J = 9/2$ decuplet is split into five Kramers doublets, as shown in Fig. 1d. Two doublets can be represented as

$$|\Gamma_{\gamma} \pm\rangle = C_1|J_z = \pm \frac{9}{2}\rangle + C_2|J_z = \pm \frac{3}{2}\rangle + C_3|J_z = \mp \frac{3}{2}\rangle, \quad (|C_1|^2 + |C_2|^2 + |C_3|^2 = 1) \quad (4)$$

and the other three as

$$|\Gamma_{\delta} \pm\rangle = C_4|J_z = \pm \frac{7}{2}\rangle + C_5|J_z = \pm \frac{1}{2}\rangle + C_6|J_z = \mp \frac{5}{2}\rangle. \quad (|C_4|^2 + |C_5|^2 + |C_6|^2 = 1), \quad (5)$$

where double-sign corresponds.

We optimize the coefficients C_i ($i = 1\sim 3$ or $4\sim 6$) to reproduce the anisotropy of $\rho(\theta, \phi)$ obtained by the CDFS analysis. The R value for the fitting of $\rho(\theta, \phi)$ is defined as

$$R = \frac{\sum_{\theta, \phi} |\rho(\theta, \phi) - s\rho_e(\theta, \phi; \Gamma)|}{\sum_{\theta, \phi} |\rho(\theta, \phi)|}. \quad (6)$$

Here, $\rho_e(\theta, \phi; \Gamma)$ is the square of the absolute value of the spherical harmonics term in the Γ state calculated by Eq. S1, as in [32], and s is the scale factor. The R values as a function of $\{C_i\}$ for $A = \text{Pr}$ and Nd are shown in two-dimensional color maps in Figs. 2c, 2e and Figs. 2g, 2i, respectively. The optimized $\{C_i\}$ parameters are listed in Tables 1 and 2. The state with the lowest R value (R_{\min}) is shown by a surface color plot in Figs. 2d, 2f, 2h and 2j. Around the Pr site, $\rho_e(\theta, \phi; \Gamma_{\alpha^+})$ (Fig. 2d) with the R_{\min} value is in better agreement with the experimental VED $\rho(\theta, \phi)$ (Fig. 2a) than $\rho_e(\theta, \phi; \Gamma_{\beta^+})$ (Fig. 2f). The obtained $\{C_i\}$ parameters for the Γ_{α^+} state are consistent with those of the lowest energy determined by the point charge model calculation considering SOC and trigonal CEF (Table 1). This finding is also consistent with previous inelastic neutron scattering measurements of $\text{Pr}_2\text{Ir}_2\text{O}_7$ [33]. Around the Nd site, $\rho_e(\theta, \phi; \Gamma_{\gamma^+})$ (Fig. 2h) is in better agreement with the experimental VED $\rho(\theta, \phi)$ (Fig. 2b) than $\rho_e(\theta, \phi; \Gamma_{\delta^+})$ (Fig. 2j), which is also consistent with the results of the point charge model calculation (Table 2). We conclude that the CDFS analysis is useful to visualize spin-orbit entangled 4f electrons and directly identify the nature of their wavefunctions from the VED distributions.

Finally, we comment on the $5d^5$ VED around the Ir^{4+} site (Fig. 3a), which has the same D_{3d} site symmetry as the A site. The $5d$ electrons around the Ir atom, which are influenced by relativistic SOC, affect the topological electronic state of this system [25-30]. Figures 3b-3d show the experimentally observed VED distributions, shown by yellow and orange iso-density surfaces with different density levels, around the Ir site of $A = \text{Pr}$, Nd , and Eu systems, respectively. Although the anisotropies of the VEDs are roughly

similar to one another, the VEDs themselves are rather erratic. Furthermore, negative VED appears near the Ir nucleus in all systems (Fig. S4b), which is unphysical. The rapid change and negative sign of VED around the Ir site may be caused by the absence of high-Q diffraction data and the narrow dynamic range of the obtained data. To observe 5d electrons, an X-ray source and diffractometer capable of ensuring a dynamic intensity range greater than 10^7 and a spatial resolution better than 0.15 Å are required (details are described in [Supplementary Information](#)).

Conclusion

The spin-orbit entangled 4f electrons around lanthanide ions in $A_2\text{Ir}_2\text{O}_7$ ($A = \text{Pr}, \text{Nd}, \text{and Eu}$) are observed by the CDFS analysis using high-photon-energy X-ray diffraction experiments. An isotropic VED distribution is observed around the Eu site, while anisotropic VED distributions are visualized around the Pr and Nd sites. The $4f^2$ electrons around the Pr site exhibit greater anisotropy than the $4f^3$ electrons around the Nd site. These anisotropies of VED around the A sites can be understood through the LS coupling scheme considering SOC and trigonal CEF. The coefficients of the linear combination of J_z eigenstates are determined by the anisotropy of the observed VED. The proposed 4f orbital observation method is applicable to various crystalline materials and can directly reveal the 4f wavefunctions.

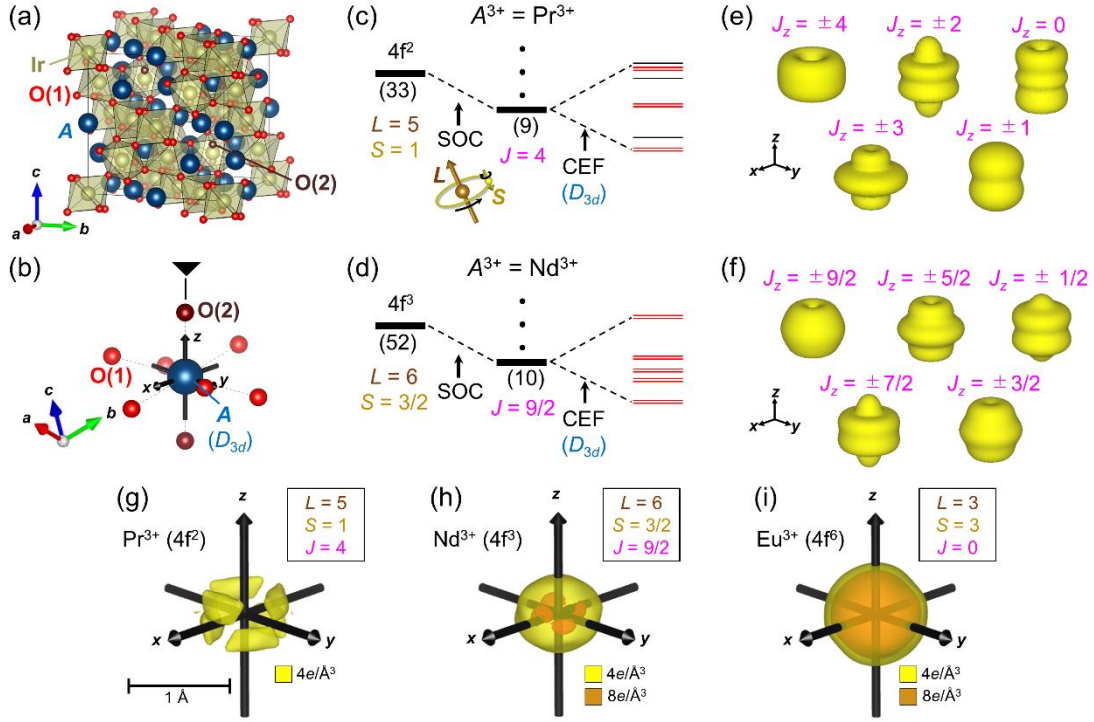


Figure 1. Crystal structure of $A_2Ir_2O_7$ and spin-orbit entangled $4f$ state on the A site. (a) Crystal structure of $A_2Ir_2O_7$. (b) A atom surrounded by eight O atoms; six O(1) and two O(2). A solid triangle indicates local three-fold rotation axis. (c),(d) Schematic of $4f^2$ and $4f^3$ states considering the SOC and trigonal CEF under the LS coupling scheme, respectively. Single black and double red lines in the right-most diagram represent singlets and doublets, respectively. (e),(f) $4f^2$ and $4f^3$ electron distributions of each J_z eigenstate in the 3H_4 ($J = 4$, $L = 5$, $S = 1$) and ${}^4I_{9/2}$ ($J = 9/2$, $L = 6$, $S = 3/2$) multiplets, respectively. (g)-(i) Experimentally obtained VED distributions around the Pr, Nd, and Eu sites, respectively. Yellow and orange iso-density surfaces show electron-density levels of 4 and $8 \text{ e}/\text{\AA}^3$, respectively.

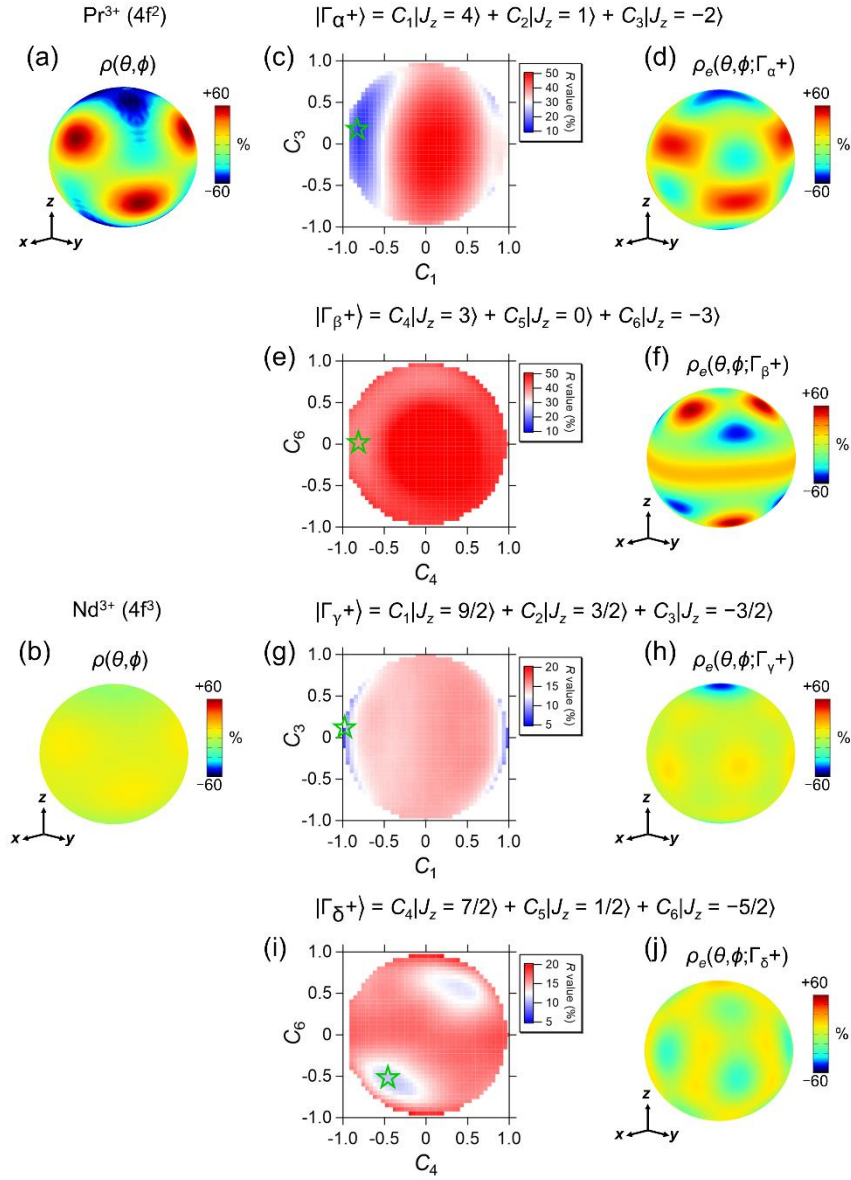


Figure 2. VED distributions around the A site. (a),(b) Direction dependence of VED distributions $\rho(\theta, \phi)$ at a distance $r = 0.33$ and 0.24 Å from the Pr and Nd sites, respectively, obtained by the CDFS analysis. The color scale indicates $[\rho(\theta, \phi) - \overline{\rho(\theta, \phi)}] / \overline{\rho(\theta, \phi)} \times 100$ [%]. (c),(e) Color maps of R values on two-dimensional C_1 — C_3 ($C_2 \geq 0$) and C_4 — C_6 ($C_5 \geq 0$) planes assuming the $|\Gamma_{\alpha^+}\rangle$ and $|\Gamma_{\beta^+}\rangle$ states of $4f^2$ electrons on a Pr³⁺ ion in the trigonal field, respectively. (d),(f) Simulated surface color plots of $\rho_e(\theta, \phi; \Gamma_{\alpha^+})$ and $\rho_e(\theta, \phi; \Gamma_{\beta^+})$, respectively. (g),(i) Color maps of R values on two-dimensional C_1 — C_3 (C_2

≥ 0) and $C_4—C_6$ ($C_5 \geq 0$) planes assuming the $|\Gamma_{\gamma^+}\rangle$ and $|\Gamma_{\delta^+}\rangle$ states of $4f^3$ electrons on an Nd^{3+} ion in the trigonal field, respectively. (h),(j) Simulated surface color plots of $\rho_e(\theta,\phi;\Gamma_{\gamma^+})$ and $\rho_e(\theta,\phi;\Gamma_{\delta^+})$, respectively. The sets of coefficients $\{C_i\}$ in (d), (f), (h), and (j) are shown by green stars in (c), (e), (g), and (i), respectively. The color bar scale is plotted as $[\rho_e(\theta,\phi;\Gamma) - N_e]/N_e \times 100$ [%]. Here, N_e is the number of $4f$ electrons.

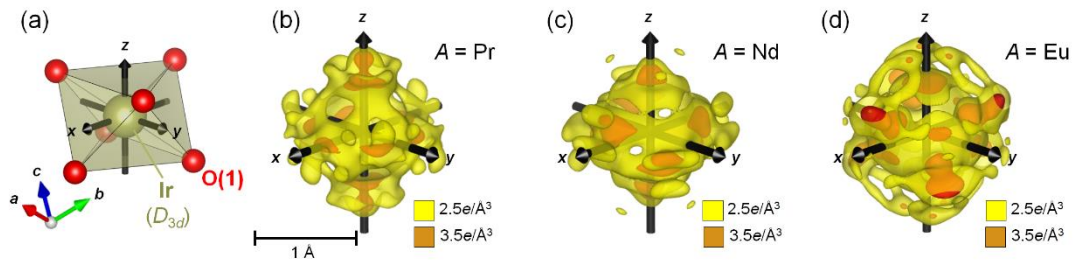


Figure 3. $5d^5$ VED around the Ir^{4+} site. (a) An Ir atom surrounded by six O(1) atoms, forming a IrO_6 octahedron. (b)-(d) Experimentally obtained VED distributions around the Ir site in $A = \text{Pr}$, Nd , and Eu systems, respectively. Yellow and orange iso-density surfaces show electron-density levels of 2.5 and $3.5 \text{ e}/\text{\AA}^3$, respectively.

Table 1. Summary of the fitting analysis of $4f^2$ VED and the point-charge model calculations of the ground state ($E = 0$) of a Pr^{3+} ion under the trigonal CEF. $|n\rangle$ denotes the state of $J = 4$ and $J_z = n$.

State	$ 4\rangle$	$ 3\rangle$	$ 2\rangle$	$ 1\rangle$	$ 0\rangle$	$ -1\rangle$	$ -2\rangle$	$ -3\rangle$	$ -4\rangle$	R_{\min} [%]
$\Gamma_{\alpha+}$	-0.79	0	0	0.60	0	0	0.15	0	0	13.13
$\Gamma_{\beta+}$	0	-0.81	0	0	0.59	0	0	0.00	0	39.36
Cal. ($E = 0$)	-0.91	0	0	0.41	0	0	0.08	0	0	

Table 2. Summary of the fitting analysis of $4f^3$ VED and the point-charge model calculations of the ground state ($E = 0$) of an Nd^{3+} ion under the trigonal CEF. $|n\rangle$ denotes the state of $J = 9/2$ and $J_z = n$.

State	$ 9/2\rangle$	$ 7/2\rangle$	$ 5/2\rangle$	$ 3/2\rangle$	$ 1/2\rangle$	$ -1/2\rangle$	$ -3/2\rangle$	$ -5/2\rangle$	$ -7/2\rangle$	$ -9/2\rangle$	R_{\min} [%]
$\Gamma_{\gamma+}$	-0.99	0	0	0.05	0	0	0.13	0	0	0	6.59
$\Gamma_{\delta+}$	0	-0.47	0	0	0.70	0	0	-0.54	0	0	10.38
Cal. ($E = 0$)	-0.96	0	0	0.07	0	0	-0.27	0	0	0	

Methods

Sample preparation

Single crystals of $A_2\text{Ir}_2\text{O}_7$ ($A = \text{Pr}, \text{Nd}, \text{and Eu}$) were grown by the KF flux method. Firstly, polycrystalline samples of them were prepared by solid-state reactions of rare-earth oxides (Pr_6O_{11} , Nd_2O_3 , and Eu_2O_3) and iridate IrO_2 . The materials with the prescribed molar ratios were ground, pressed into a pellet, and sintered at 1000 °C for several days. The sintered polycrystals were ground and mixed with KF in a ratio of 1:200. The mixtures were placed in a platinum crucible covered with a lid. The crucible was cooled down to 850 °C at a rate of 2 °C/hour following anneal at 1100 °C for 5 h. After

cooling to room temperature, crystals were separated from the KF residual flux by rinsing with distilled water. Octahedron-shaped single crystals were obtained.

X-ray diffraction experiments

X-ray diffraction experiments were performed on BL02B1 at a synchrotron facility SPring-8, Japan [34]. An N₂-gas-blowing device was employed to cool the crystals to 100 K. A two-dimensional detector CdTe PILATUS, which had a dynamic range exceeding 10⁶, was used to record the diffraction pattern. The X-ray wavelength was calibrated to be $\lambda = 0.30946 \text{ \AA}$. The intensities of Bragg reflections of the interplane distance $d > 0.28 \text{ \AA}$ were collected by CrysAlisPro program [35] using a fine slice method, in which the data were obtained by dividing the reciprocal space region in increments of $\Delta\omega = 0.01^\circ$. Intensities of equivalent reflections were averaged and the structural parameters were refined by using Jana2006 [36]. The X-ray diffraction experiments of A₂Ir₂O₇ (A = Pr, Nd, and Eu) detected no structural phase transitions down to 100 K, which was consistent with the previous X-ray diffraction experiments [20]. The structural analysis found no significant off-stoichiometry at each atomic site. Here, the structural refinement was performed using only high-angle reflections of $\sin\theta/\lambda > 0.6 \text{ \AA}^{-1}$. Since the contribution of spatially spread valence electrons to X-ray diffraction is negligible in the high-angle region [12], the structural parameters including the atomic displacement parameters are obtained with high accuracy. The detailed structural parameters of A₂Ir₂O₇ are summarized in Tables S1-S6.

Point-charge model calculations

The CEF energies via the point charge model in the limit of strong spin-orbit interactions were calculated by the software package PyCrystalField [37] using the obtained crystal structures.

CDFS analysis

The CDFS method [10] was used to extract the VED distribution around each atomic site at 100 K. [He]-, [Xe]- and ([Xe] 4f¹⁴)-type electron configurations were regarded as core electrons for O, lanthanide (Pr, Nd, and Eu), and Ir atoms, respectively. The effect of the thermal vibration was subtracted from the VED using the atomic displacement parameters determined by the high-angle analysis. The voxel size of the three-dimensional electron density distribution was set to be $\Delta V = (0.02 \text{ \AA})^3$. It should be noted that the absolute value of the obtained VED does not directly reproduce the number of valence electrons around the atoms because the effect of double scattering, absorption, extinction, and detector saturation could not be completely excluded in the measurement of diffraction intensities. Crystal structure and ED distribution were visualized by using VESTA [38].

DFT calculations

To obtain the atomic form factors for the CDFS analysis, we performed fully relativistic all-electron calculations based on the density functional theory (DFT) for isolated O, Pr, Nd, Eu, and Ir atoms using Quantum ESPRESSO [39]. The Perdew-Burke-Ernzerhof functional [40] was employed to approximate the exchange-correlation functional. The obtained radial distribution functions of each orbital of Pr, Nd, Eu, and Ir atoms are summarized in Fig. S2.

Acknowledgements

We thank H. Kusunose for fruitful discussions. This work was supported by a Grant-in-Aid for Scientific Research (No. 22K14010, 23K03307, 23H04869, 24H01644, 24H01649, and 24K00582) from JSPS. This work was supported by the RIKEN TRIP

initiative (RIKEN Quantum, Advanced General Intelligence for Science Program, Many-body Electron Systems). The synchrotron radiation experiments were performed at SPring-8 with the approval of the Japan Synchrotron Radiation Research Institute (JASRI) (Proposal No. 2022A1751, 2022B1582, 2023A1687, and 2023B1603).

Author contributions

S.K. and T.A. designed and coordinated the study. K. U. and Y. T. grew the crystal; S.K., Y.Na., and K.S. performed the XRD experiment; S.K. analyzed the XRD data; Y.No. and R.A. performed the DFT calculation. S.K. and T.A. wrote the manuscript. All authors discussed the experimental results and contributed to the manuscript.

Competing interests

The authors declare no competing interests.

References

1. Elliott, R. *Magnetic Properties of Rare Earth Metals* (Springer Science & Business Media, New York, (2013).
2. Kuramoto, Y., Kusunose, H. & Kiss, A. Multipole Orders and Fluctuations in Strongly Correlated Electron Systems. *J. Phys. Soc. Jpn.* **78**, 072001 (2009).
3. Yuan, H. Q., Grosche, F. M., Deppe, M., Geibel, C., Sparn, G. & Steglich, F. Observation of Two Distinct Superconducting Phases in CeCu_2Si_2 . *Science* **302**, 2104-2107 (2003).
4. Onimaru, T., Matsumoto, K. T., Inoue, Y. F., Umeo, K., Saiga, Y., Matsushita, Y., Tamura, R., Nishimoto, K., Ishii, I., Suzuki, T. & Takabatake, T. Superconductivity and Structural Phase Transitions in Caged Compounds $RT_2\text{Zn}_{20}$ ($R = \text{La, Pr}$, $T = \text{Ru, Ir}$). *J. Phys. Soc. Jpn.* **79**, 033704 (2010).

5. Kondo, J. Resistance Minimum in Dilute Magnetic Alloys. *Progress of theoretical physics* **32**, 37-49 (1964).
6. Ito, Y. & Akimitsu, J. Observation of orbital ordering in K_2CuF_4 . *J. Phys. Soc. Jpn.* **40**, 1333 (1976).
7. Streltsov, V. A., Belokoneva, E. L., Tsirelson, V. G. & Hansen, N. K. Multipole analysis of the electron density in triphylite, $LiFePO_4$, using X-ray diffraction data. *Acta Cryst.* **B49**, 147-153 (1993).
8. Murakami, Y., Hill, J. P., Gibbs, D., Blume, M., Koyama, I., Tanaka, M., Kawata, H., Arima, T., Tokura, Y., Hirota, K. & Endoh, Y. Resonant X-Ray Scattering from Orbital Ordering in $LaMnO_3$. *Phys. Rev. Lett.* **81**, 582 (1998).
9. Yavaş, H., Sundermann, M., Chen, K., Amorese, A., Severing, A., Gretarsson, H., Haverkort, M. W. & Tjeng, L. H. Direct imaging of orbitals in quantum materials. *Nat. Phys.* **15**, 559 (2019).
10. Kitou, S., Manjo, T., Katayama, N., Shishidou, T., Arima, T., Taguchi, Y., Tokura, Y., Nakamura, T., Yokoyama, T., Sugimoto, K. & Sawa, H. Collapse of the simple localized $3d^1$ orbital picture in Mott insulator. *Phys. Rev. Research* **2**, 033503 (2020).
11. Gao, C., Genoni, A., Gao, S., Jiang, S., Soncini, A. & Overgaard, J. Observation of the asphericity of 4f-electron density and its relation to the magnetic anisotropy axis in single-molecule magnets. *Nat. Chem.* **12**, 213-219 (2020).
12. Kitou, S., Fujii, T., Kawamoto, T., Katayama, N., Maki, S., Nishibori, E., Sugimoto, K., Takata, M., Nakamura, T. & Sawa, H. Successive Dimensional Transition in $(TMTTF)_2PF_6$ Revealed by Synchrotron X-ray Diffraction. *Phys. Rev. Lett.* **119**, 065701 (2017).
13. Kitou, S., Hosogi, Y., Kitaura, R., Naito, T., Nakamura, T. & Sawa, H. Direct

- Observation of Molecular Orbitals Using Synchrotron X-ray Diffraction. *Crystals* **10**, 998 (2020).
14. Manjo, T., Kitou, S., Katayama, N., Nakamura, S., Katsufuji, T., Nii, Y., Arima, T., Nasu, J., Hasegawa, T., Sugimoto, K., Ishikawa, D., Baron, A. Q. E. & Sawa, H. Do electron distributions with orbital degree of freedom exhibit anisotropy? *Mater. Adv.* **2**, 3192-3198 (2022).
 15. Kitou, S., Kaneko, Y., Nakamura, Y., Sugimoto, K., Nomura, Y., Arita, R., Tokura, Y., Sawa, H. & Arima, T. Visualization of 4d orbital electrons in a pyrochlore-type oxide. *Phys. Rev. B* **108**, 024103 (2023).
 16. Kitou, S., Gen, M., Nakamura, Y., Sugimoto, K., Tokunaga, Y., Ishiwata, S. & Arima, T. Real-Space Observation of Ligand Hole State in Cubic Perovskite SrFeO₃. *Adv. Sci.* **10**, 2302839 (2023).
 17. Kitou, S., Nakano, A., Imaizumi, M., Nakamura, Y., Terasaki, I., & Arima, T. Molecular orbital formation and metastable short-range ordered structure in VO₂. *Phys. Rev. B* **109**, L100101 (2024).
 18. Hara, T., Hasebe, M., Tsuneda, T., Naito, T., Nakamura, Y., Katayama, N., Taketsugu, T., & Sawa, H. Unveiling the Nature of Chemical Bonds in Real Space. *J. Am. Chem. Soc.* **146**, 23825 (2024).
 19. Sleight, A. W. New ternary oxides of Re, Os, Ir and Pt with cubic crystal structures. *Solid State Commun.* **9**, 1177 (1974).
 20. Takatsu, H., Watanabe, K., Goto, K. & Kadowaki, H. Comparative study of low-temperature x-ray diffraction experiments on R₂Ir₂O₇ (R = Nd, Eu, and Pr). *Phys. Rev. B* **90**, 235110 (2014).
 21. Yanagishima, D. & Maeno, Y. Metal-Nonmetal Changeover in Pyrochlore Iridates. *J.*

- Phys. Soc. Jpn.* **70**, 2880-2883 (2001).
22. Matsuhira, K., Wakeshima, M., Nakanishi, R., Yamada, T., Nakamura, A., Kawano, W., Takagi, S. & Hinatsu, Y. Metal–Insulator Transition in Pyrochlore Iridates $Ln_2Ir_2O_7$ ($Ln = Nd, Sm, \text{ and } Eu$). *J. Phys. Soc. Jpn.* **76**, 043706 (2007).
 23. Matsuhira, K., Wakeshima, M., Hinatsu, Y. & Takagi, S. Metal–Insulator Transition in Pyrochlore Oxides $Ln_2Ir_2O_7$. *J. Phys. Soc. Jpn.* **80**, 094701 (2011).
 24. Ueda, K., Fujioka, J. & Tokura, Y. Variation of optical conductivity spectra in the course of bandwidth-controlled metal-insulator transitions in pyrochlore iridates. *Phys. Rev. B* **93**, 245120 (2016).
 25. Machida, Y., Nakatsuji, S., Maeno, Y., Tayama, T., Sakakibara, T. & Onoda, S. Unconventional Anomalous Hall Effect Enhanced by a Noncoplanar Spin Texture in the Frustrated Kondo Lattice $Pr_2Ir_2O_7$. *Phys. Rev. Lett.* **98**, 057203 (2007).
 26. Machida, Y., Nakatsuji, S., Onoda, S., Tayama, T. & Sakakibara, T. Time-reversal symmetry breaking and spontaneous Hall effect without magnetic dipole order. *Nature* **463**, 210 (2010).
 27. Ueda, K., Kaneko, R., Ishizuka, H., Fujioka, J., Nagaosa, N. & Tokura, Y. Spontaneous Hall effect in the Weyl semimetal candidate of all-in all-out pyrochlore iridate. *Nat. Commun.* **9**, 3032 (2018).
 28. Ueda, K., Fujioka, J., Yang, B.-J., Shiogai, J., Tsukazaki, A., Nakamura, S., Awaji, S., Nagaosa, N. & Tokura, Y. Magnetic Field-Induced Insulator-Semimetal Transition in a Pyrochlore $Nd_2Ir_2O_7$. *Phys. Rev. Lett.* **115**, 056402 (2015).
 29. Nakatsuji, S., Machida, Y., Maeno, Y., Tayama, T., Sakakibara, T., Duijn, J. van, Balicas, L., Millican, J. N., Macaluso, R. T. & Chan, Julia Y. Metallic Spin-Liquid Behavior of the Geometrically Frustrated Kondo Lattice $Pr_2Ir_2O_7$. *Phys. Rev. Lett.* **96**,

- 087204 (2006).
30. Ueda, K., Ishizuka, H., Kriener, M., Kitou, S., Maryenko, D., Kawamura, M., Arima, T., Kawasaki, M. & Tokura, Y. Experimental signatures of a versatile Weyl semimetal in a pyrochlore iridate with spin-ice-like magnetic orders. *Phys. Rev. B* **105**, L161102 (2022).
 31. Hutchings, M. T. Point-charge calculations of energy levels of magnetic ions in crystalline electric fields. *Solid State Phys.* **16**, 227 (1964).
 32. Kusunose, H. Description of multipole in f-electron systems. *J. Phys. Soc. Jpn.* **77**, 064710 (2008).
 33. Machida, Y., Nakatsuji, S., Tonomura, H., Toyama, T., Sakakibara, T., van Dujin, J., Broholm, C. & Maeno, Y. Crystalline electric field levels and magnetic properties of the metallic pyrochlore compound $\text{Pr}_2\text{Ir}_2\text{O}_7$. *J. Phys. Chem. Solids* **66**, 1435-1437 (2005).
 34. Sugimoto, K., Ohsumi, H., Aoyagi, S., Nishibori, E., Moriyoshi, C., Kuroiwa, Y., Sawa, H. & Takata, M. Extremely High Resolution Single Crystal Diffractometry for Orbital Resolution using High Energy Synchrotron Radiation at SPring-8. *AIP Conf. Proc.* **1234**, 887 (2010).
 35. CrysAlisPro, Agilent Technologies Ltd, Yarnton, Oxfordshire, England, (2014).
 36. Petříček, V., Dušek, M. & Palatinus, L. Crystallographic Computing System JANA2006: General features. *Z. Kristallogr. Cryst. Mater.* **229**, 345 (2014).
 37. Scheie, A. PyCrystalField: Software for Calculation, Analysis and Fitting of Crystal Electric Field Hamiltonians. *J. Appl. Cryst.* **54**, 356 (2021).
 38. Momma, K. & Izumi, F. VESTA 3 for three-dimensional visualization of crystal, volumetric and morphology data. *J. Appl. Crystallogr.* **44**, 1272 (2011).

39. Giannozzi, P. *et al.*, Advanced capabilities for materials modeling with QUANTUM ESPRESSO. *J. Phys.: Condens. Matter* **29**, 465901 (2017).
40. Perdew, J. P., Burke, K. & Ernzerhof, M. Generalized Gradient Approximation Made Simple. *Phys. Rev. Lett.* **77**, 3865-3868 (1996).

Supplementary Information of
Visualization of spin-orbit entangled 4f electrons

Shunsuke Kitou¹, Kentaro Ueda², Yuiga Nakamura³, Kunihisa Sugimoto⁴,
Yusuke Nomura⁵, Ryotaro Arita^{6,7}, Yoshinori Tokura^{2,7,8}, and Taka-hisa Arima^{1,7}

¹*Department of Advanced Materials Science, The University of Tokyo, Kashiwa 277-8561, Japan*

²*Department of Applied Physics, The University of Tokyo, Tokyo 113-8656, Japan*

³*Japan Synchrotron Radiation Research Institute (JASRI), SPring-8, Hyogo 679-5198, Japan*

⁴*Department of Chemistry, Kindai University, Osaka 577-8502, Japan*

⁵*Institute for Materials Research, Tohoku University, Sendai, 980-8577, Japan*

⁶*Department of Physics, The University of Tokyo, Tokyo 113-0033, Japan*

⁷*RIKEN Center for Emergent Matter Science (CEMS), Wako 351-0198, Japan*

⁸*Tokyo College, The University of Tokyo, Tokyo 113-8656, Japan*

1. Crystal structures and VED distributions of $A_2\text{Ir}_2\text{O}_7$ at 100 K

The results of the structural analysis of $A_2\text{Ir}_2\text{O}_7$ ($A = \text{Pr}, \text{Nd}, \text{and Eu}$) at 100 K are summarized in [Tables S1-S6](#) and [Fig. S1](#). [Figure S2](#) shows radial distribution functions of each orbital for isolated neutral Pr, Nd, Eu, and Ir atoms, obtained by density-functional-theory (DFT) calculations. These functions were used to calculate the core electron density for the core differential Fourier synthesis (CDFS) analysis.

[Figure S3](#) shows one-dimensional plots of valence electron density (VED) around the $A = \text{Pr}, \text{Nd}, \text{and Eu}$ sites in $A_2\text{Ir}_2\text{O}_7$. [Figure S4](#) shows one-dimensional plots of calculated and experimental VED around the Ir site in $A = \text{Pr}, \text{Nd}, \text{and Eu}$ systems. Since the 5d orbital has two radial nodes corresponding to the sign switching point of the radial wavefunction, it is expected that two dip structures appear in the radial distribution of electron density. A black line in [Fig. S4a](#) shows the one-dimensional plot of the $5d_{xy}$ VED obtained by DFT calculations against the distance r from the nucleus in the $[110]$ direction, where two dip structures exist around $r = 0.1$ and 0.3 \AA . It is noted that the experimentally observed VED distribution has limited spatial resolution depending on the minimum interplane distance d_{min} of the diffraction data. Purple and red lines in [Fig. S4a](#) represent the one-dimensional plots of the calculated $5d_{xy}$ VED, incorporating resolutions $d_{\text{min}} = 0.15$ and 0.28 \AA , respectively (details of the calculation method are explained in Chapter 3). Notably, $d_{\text{min}} = 0.28 \text{ \AA}$ aligns with the actual resolution of the data obtained from the present X-ray diffraction measurement. While the two dip positions can be identified in the VED with $d_{\text{min}} = 0.15 \text{ \AA}$, the dip close to the nucleus cannot be observed in the VED with $d_{\text{min}} = 0.28 \text{ \AA}$.

Black, green, and blue dots in [Fig. S4b](#) show one-dimensional plots of the observed VED around the Ir site of $A = \text{Pr}, \text{Nd}, \text{and Eu}$ systems, respectively, against the distance r from the nucleus along the z -axis (three-fold rotation axis). Their VED distributions around $r = 0.55 \text{ \AA}$, outside of the two nodes, are roughly similar to the calculated radial distribution considering the experimental resolution with $d_{\text{min}} = 0.28 \text{ \AA}$. The anisotropy of the spherical harmonics term of the VED around $r = 0.55 \text{ \AA}$ is much smaller than those of the isolated IrO_6 cluster model calculation considering trigonal point-charge electric field and spin-orbit coupling ([Fig. S5](#)). This is because the VED of the outermost 5d orbital may be modified through the hybridizations with the 2p orbital of the surrounding oxygen ions. To evaluate the anisotropy of the 5d orbital, it is necessary to correctly observe the anisotropy around $r = 0.2 \text{ \AA}$. Furthermore, unphysical negative VED appears near the Ir nucleus in all systems. The observation of 5d electrons requires X-ray source and diffractometer capable of ensuring the dynamic range of intensity greater than 10^7 and a spatial resolution better than 0.15 \AA .

2. Electron density calculation of the 4f state

In the *LS* coupling scheme, the total orbital and spin angular momentum quantum numbers, L and S , are first considered as eigenvalues. Then, S and L couple to form a total angular momentum J . The electron density in the Γ state is described as

$$\rho_e(\mathbf{r}; \Gamma) = -eR_f^2(r)\rho_e(\theta, \phi; \Gamma)/4\pi,$$

$$\rho_e(\theta, \phi; \Gamma) = \sum_{l=0}^6 (2l+1) g_n^{(l)} \langle J || \hat{J}_l || J \rangle \sum_{m=-l}^l W_{lm}(\Gamma) Z_{lm}(\theta, \phi). \quad (\text{S1})$$

Here, $g_n^{(l)}$ is Stevens' factor, $Z_{lm}(\theta, \phi)$ is tesseral harmonics,

$$\langle J || \hat{J}_l || J \rangle = \frac{1}{2^l} \sqrt{\frac{(2J+l+1)!}{(2J-l)!}},$$

$$W_{lm}(\Gamma) = \sum_{J_z J_z'} (-1)^{J+J_z-l} \begin{pmatrix} J & J & l \\ -J_z' & J_z & m \end{pmatrix} U_{J_z' \Gamma}^* U_{J_z \Gamma},$$

where $U_{J_z \Gamma}$ is a unitary matrix of an arbitrary state within the J multiplet,

$$|\Gamma\rangle = \sum_{J_z} U_{J_z \Gamma} |J, J_z\rangle.$$

The detail for the calculation method is given in Ref. [1].

3. Electron density considering the experimental resolution

The experimentally observed electron density distribution has limited spatial resolution depending on the minimum interplane distance d_{\min} of the diffraction data. To compare the calculated 5d electron density $\rho(d_{\min} = 0 \text{ \AA})$ with experimental data at the spatial resolution $d_{\min} = 0.28 \text{ \AA}$, the 5d electron density was calculated using the following process. (i) The crystal structure factor $F(\mathbf{K})$ was calculated by the Fourier transform of $\rho(d_{\min} = 0 \text{ \AA})$ as

$$F(\mathbf{K}) = \int_{\text{unit cell}} \rho(d_{\min} = 0 \text{ \AA}) e^{-i\mathbf{K}\cdot\mathbf{r}} d\mathbf{r}. \quad (\text{S2})$$

(ii) $\rho(d_{\min} = 0.28 \text{ \AA})$ was calculated by the inverse Fourier transform of the calculated $F(\mathbf{K})$ with $d_{\min} = 0.28 \text{ \AA}$ using

$$\rho(d_{\min} = 0.28 \text{ \AA}) = \frac{1}{V} \sum_{|\mathbf{K}| \leq |\mathbf{K}|_{\max}} F(\mathbf{K}) e^{i\mathbf{K}\cdot\mathbf{r}}. \quad (\text{S3})$$

Here, $|\mathbf{K}|_{\max} = 2\pi/d_{\min}$.

4. Calculation of crystal electric field splitting

We used the software package PyCrystalField [2] for the calculation of crystal electric field splitting via the point charge model in the limit of strong spin-orbit interactions. Tables S7 and S8 show the calculated $J = 4$ and $9/2$ multiplet states of $\text{Pr}^{3+} 4f^2$ and $\text{Nd}^{3+} 4f^3$, respectively. Only eight O^{2-} ions around the A^{3+} ions were considered in the calculation.

Table S1. Structural parameters of Pr₂Ir₂O₇ at 100 K. The space group is *Fd-3m* and $a = 10.3834(9)$ Å.

Atom	Wyckoff position	Site symmetry	x	y	z
Pr	16 <i>d</i>	.-3 <i>m</i>	1/2	1/2	1/2
Ir	16 <i>c</i>	.-3 <i>m</i>	0	0	0
O(1)	48 <i>f</i>	2. <i>mm</i>	0.33119(3)	1/8	1/8
O(2)	8 <i>b</i>	-43 <i>m</i>	3/8	3/8	3/8
Atom	U_{11} (Å ²)	$U_{22} = U_{33}$ (Å ²)	$U_{12} = U_{13}$ (Å ²)	U_{23} (Å ²)	
Pr	0.002409(12)	= U_{11}	-0.000343(3)	= U_{12}	
Ir	0.001551(9)	= U_{11}	-0.000035(2)	= U_{12}	
O(1)	0.00404(6)	0.00389(3)	0	0.00114(5)	
O(2)	0.00368(5)	= U_{11}	0	0	

Table S2. Summary of crystallographic data of Pr₂Ir₂O₇ at 100 K.

Wavelength (Å)	0.30946
Crystal dimension (μm ³)	20 × 20 × 20
Space group	<i>Fd-3m</i>
a (Å)	10.3834(9)
Z	8
$F(000)$	2624
$(\sin\theta/\lambda)_{\max}$ (Å ⁻¹)	1.79
N_{total}	42143
N_{unique}	1315
Average redundancy	32.048
Completeness (%)	97.84
Number of unique reflections ($I > 3\sigma$ / all)	1052 / 1315
$N_{\text{parameters}}$	10
R_1 ($I > 3\sigma$ / all) (%)	1.97 / 2.21
wR_2 ($I > 3\sigma$ / all) (%)	2.41 / 2.49
GOF ($I > 3\sigma$ / all)	1.68 / 1.55

Table S3. Structural parameters of Nd₂Ir₂O₇ at 100 K. The space group is *Fd-3m* and *a* = 10.3613(7) Å.

Atom	Wyckoff position	Site symmetry	<i>x</i>	<i>y</i>	<i>z</i>
Nd	16 <i>d</i>	.-3 <i>m</i>	1/2	1/2	1/2
Ir	16 <i>c</i>	.-3 <i>m</i>	0	0	0
O(1)	48 <i>f</i>	2. <i>mm</i>	0.33195(3)	1/8	1/8
O(2)	8 <i>b</i>	-43 <i>m</i>	3/8	3/8	3/8
Atom	<i>U</i> ₁₁ (Å ²)	<i>U</i> ₂₂ = <i>U</i> ₃₃ (Å ²)	<i>U</i> ₁₂ = <i>U</i> ₁₃ (Å ²)	<i>U</i> ₂₃ (Å ²)	
Nd	0.002262(12)	= <i>U</i> ₁₁	-0.000348(3)	= <i>U</i> ₁₂	
Ir	0.001411(10)	= <i>U</i> ₁₁	-0.000037(2)	= <i>U</i> ₁₂	
O(1)	0.00373(6)	0.00370(4)	0	0.00109(5)	
O(2)	0.00342(6)	= <i>U</i> ₁₁	0	0	

Table S4. Summary of crystallographic data of Nd₂Ir₂O₇ at 100 K.

Wavelength (Å)	0.30946
Crystal dimension (μm ³)	30 × 25 × 25
Space group	<i>Fd-3m</i>
<i>a</i> (Å)	10.3613(7)
<i>Z</i>	8
<i>F</i> (000)	2640
(sinθ/λ) _{max} (Å ⁻¹)	1.79
<i>N</i> _{total}	42506
<i>N</i> _{unique}	1318
Average redundancy	32.25
Completeness (%)	98.95
Number of unique reflections (<i>I</i> >3σ / all)	1056/ 1318
<i>N</i> _{parameters}	10
<i>R</i> ₁ (<i>I</i> >3σ / all) (%)	1.42 / 1.76
<i>wR</i> ₂ (<i>I</i> >3σ / all) (%)	2.23 / 2.37
GOF (<i>I</i> >3σ / all)	1.46 / 1.39

Table S5. Structural parameters of $\text{Eu}_2\text{Ir}_2\text{O}_7$ at 100 K. The space group is $Fd-3m$ and $a = 10.2744(8)$ Å.

Atom	Wyckoff position	Site symmetry	x	y	z
Eu	16 <i>d</i>	.-3 <i>m</i>	1/2	1/2	1/2
Ir	16 <i>c</i>	.-3 <i>m</i>	0	0	0
O(1)	48 <i>f</i>	2. <i>mm</i>	0.33441(3)	1/8	1/8
O(2)	8 <i>b</i>	-43 <i>m</i>	3/8	3/8	3/8
Atom	U_{11} (Å ²)	$U_{22} = U_{33}$ (Å ²)	$U_{12} = U_{13}$ (Å ²)	U_{23} (Å ²)	
Eu	0.002330(13)	= U_{11}	-0.000320(3)	= U_{12}	
Ir	0.001565(11)	= U_{11}	-0.000036(2)	= U_{12}	
O(1)	0.00399(7)	0.00378(4)	0	0.00092(6)	
O(2)	0.00355(6)	= U_{11}	0	0	

Table S6. Summary of crystallographic data of $\text{Eu}_2\text{Ir}_2\text{O}_7$ at 100 K.

Wavelength (Å)	0.30946
Crystal dimension (μm^3)	30 × 20 × 10
Space group	$Fd-3m$
a (Å)	10.2744(8)
Z	8
$F(000)$	2688
$(\sin\theta/\lambda)_{\text{max}}$ (Å ⁻¹)	1.79
N_{total}	41390
N_{unique}	1280
Average redundancy	32.336
Completeness (%)	98.23
Number of unique reflections ($I > 3\sigma$ / all)	1038/ 1280
$N_{\text{parameters}}$	10
R_1 ($I > 3\sigma$ / all) (%)	1.67 / 2.03
wR_2 ($I > 3\sigma$ / all) (%)	2.39 / 2.59
GOF ($I > 3\sigma$ / all)	1.58 / 1.54

Table S7. Calculated $J = 4$ states of $\text{Pr}^{3+} 4f^2$ in $\text{Pr}_2\text{Ir}_2\text{O}_7$ at 100 K.

E (meV)	4⟩	3⟩	2⟩	1⟩	0⟩	-1⟩	-2⟩	-3⟩	-4⟩
0	-0.91	0	0	0.41	0	0	0.08	0	0
0	0	0	0.08	0	0	-0.41	0	0	-0.91
15.63	0	0.16	0	0	-0.98	0	0	-0.16	0
66.41	-0.14	0	-0.01	-0.30	0	-0.86	0.01	0	0.39
66.41	-0.39	0	0.01	-0.86	0	0.30	0.01	0	-0.14
101.19	0	-0.69	0	0	-0.22	0	0	0.69	0
116.75	-0.08	0	0.16	0.02	0	0.00	-0.98	0	0.01
116.75	0.01	0	0.98	0.00	0	0.02	0.16	0	0.08
120.25	0	-0.71	0	0	0.00	0	0	-0.71	0

Table S8. Calculated $J = 9/2$ states of $\text{Nd}^{3+} 4f^3$ in $\text{Nd}_2\text{Ir}_2\text{O}_7$ at 100 K.

E (meV)	9/2⟩	7/2⟩	5/2⟩	3/2⟩	1/2⟩	-1/2⟩	-3/2⟩	-5/2⟩	-7/2⟩	-9/2⟩
0	0	0	0	0.27	0	0	0.07	0	0	0.96
0	-0.96	0	0	0.07	0	0	-0.27	0	0	0
20.07	0	-0.03	-0.37	0	0.17	0.90	0	0.07	0.14	0
20.07	0	-0.14	0.07	0	0.90	-0.17	0	0.37	-0.03	0
30.50	0.03	0	0	-0.90	0	0	-0.34	0	0	0.28
30.50	-0.28	0	0	-0.34	0	0	0.90	0	0	0.03
44.81	0	-0.12	-0.82	0	0.08	-0.27	0	-0.23	-0.43	0
44.81	0	0.43	-0.23	0	-0.27	-0.08	0	0.82	-0.12	0
85.68	0	-0.89	-0.01	0	-0.29	-0.01	0	0.37	0.01	0
85.68	0	-0.01	0.37	0	-0.01	0.29	0	0.01	-0.89	0

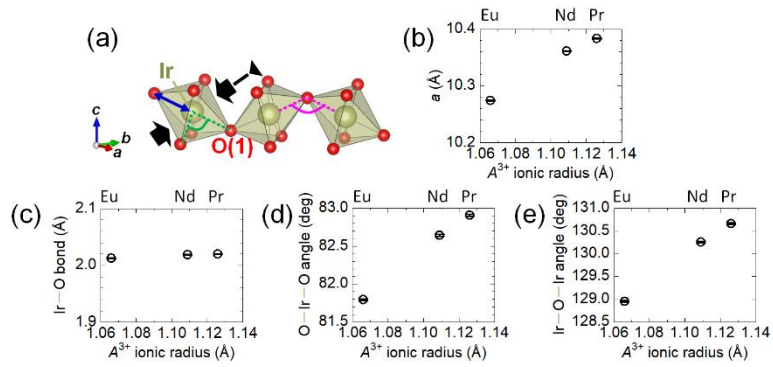


Figure S1. Crystal structure of $A_2\text{Ir}_2\text{O}_7$ ($A = \text{Pr}, \text{Nd}, \text{and Eu}$) at 100 K. (a) A one-dimensional chain of IrO_6 octahedra. *A*-ion dependence of (b) lattice constant, (c) Ir—O bond length, (d) O—Ir—O angle, and (e) Ir—O—Ir angle.

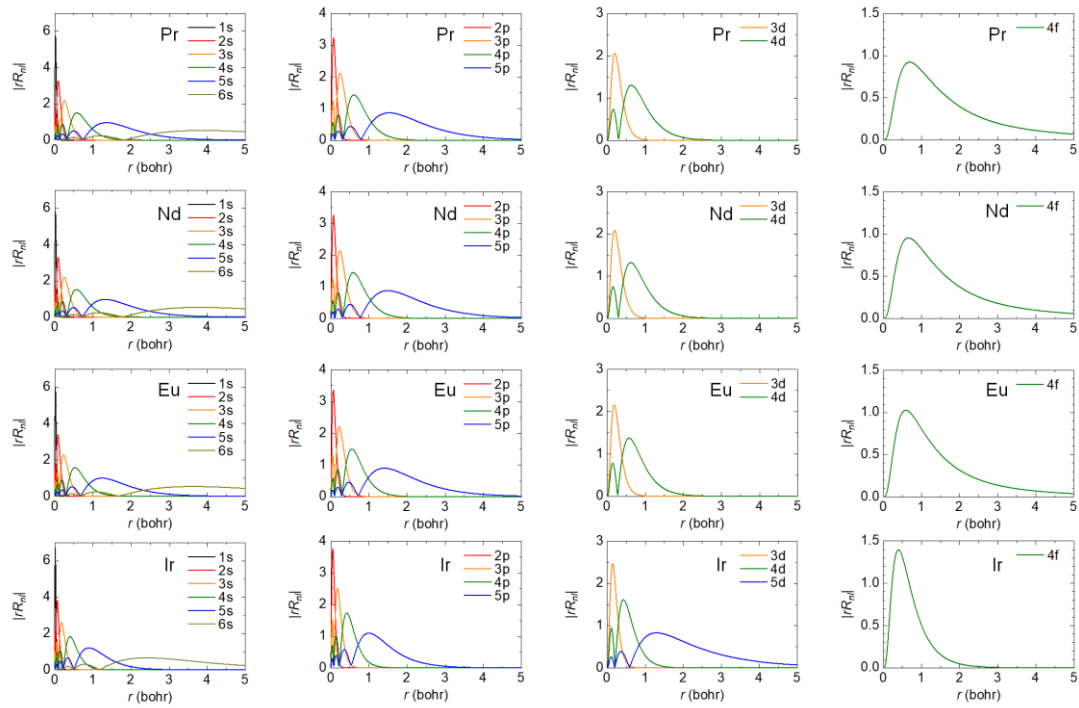


Figure S2. Radial distribution functions of each orbital for isolated neutral Pr, Nd, Eu, and Ir atoms obtained by density-functional-theory calculations.

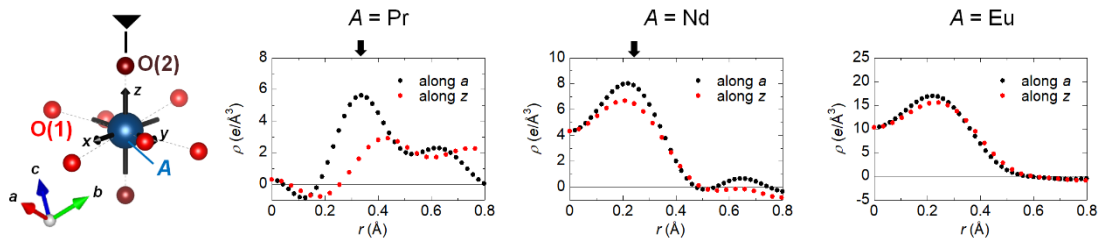


Figure S3. One-dimensional plots of VED around the Pr, Nd, and Eu sites along the *a*- and *z*-axes.

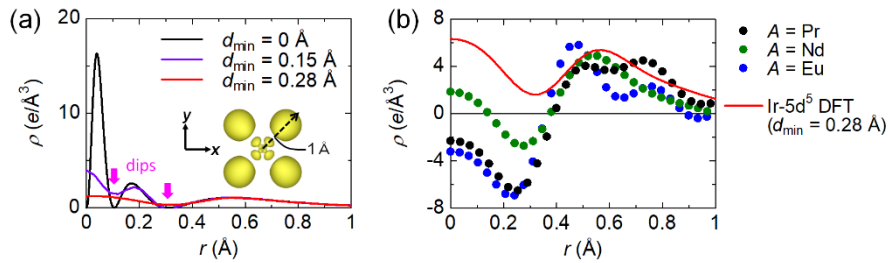


Figure S4. One-dimensional plots of calculated and experimental VED around the Ir site in *A* = Pr, Nd, and Eu systems. (a) A black line shows the Ir $5d_{xy}$ VED, calculated by the density functional theory, as a function of the distance r from the Ir nucleus in the $[110]$ direction. Purple and red lines show the calculated $5d_{xy}$ VED, incorporating resolutions $d_{\min} = 0.15$ and 0.28 Å, respectively. The inset in (a) shows the calculated Ir $5d_{xy}$ VED distribution, where yellow iso-density surfaces show electron-density levels of 0.3 $e/\text{Å}^3$. (b) Black, green, and blue dots show the experimental VED around the Ir site of *A* = Pr, Nd, and Eu ions, respectively, against the distance r from the nucleus along the *z*-axis (three-fold rotation axis). A red line shows the calculated $5d_{xy}$ VED incorporating resolutions $d_{\min} = 0.28$ Å.

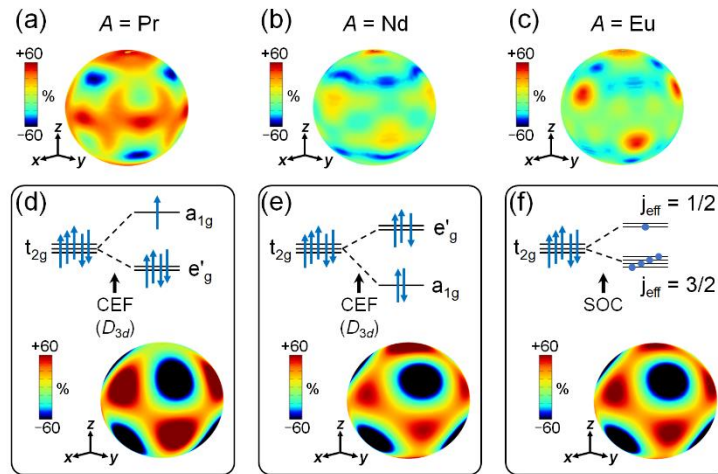


Figure S5. (a)-(c) Observed VED distributions $\rho(\theta, \phi)$ at a distance $r = 0.55 \text{ \AA}$ from the Ir site in the $A = \text{Pr}$, Nd , and Eu systems, respectively. The color scale indicates $[\rho(\theta, \phi) - \overline{\rho(\theta, \phi)}] / \overline{\rho(\theta, \phi)} \times 100$ [%]. (d)-(f) Calculated anisotropies of the spherical harmonics term around the Ir site considering (d) strong trigonal crystal electric field (CEF) and the a_{1g} singlet lies higher energy than the e'_g doublet, (e) strong trigonal CEF which produces the e'_g doublet energy higher than the a_{1g} singlet, and (f) strong spin-orbit coupling (SOC), respectively. The color bar scale is plotted as $[\rho_e(\theta, \phi) - N_e] / N_e \times 100$ [%]. Here, $N_e = 5$ is the number of 5d electrons.

References

1. Kusunose, H. Description of multipole in f-electron systems. *J. Phys. Soc. Jpn.* **77**, 064710 (2008).
2. Scheie, A. PyCrystalField: Software for Calculation, Analysis and Fitting of Crystal Electric Field Hamiltonians. *J. Appl. Cryst.* **54**, 356 (2021).